remote sensing

MDPI

Article

Monitoring Building Activity by Persistent Scatterer Interferometry

Vasilis Letsios [1,*], Ioannis Faraslis [2] and Demetris Stathakis [1]

[1] Spatial Analysis, GIS and Thematic Mapping Laboratory, Department of Planning and Regional Development, University of Thessaly, 38334 Volos, Greece
[2] Department of Environmental Sciences, University of Thessaly, 41222 Larisa, Greece
* Correspondence: vletsios@uth.gr; Tel.: +30-24210-74426

Abstract: In many countries globally, information for new buildings is either scarce or incomplete. In an effort to bridge this information gap an approach based on public domain synthetic aperture radar (SAR) satellite data is introduced. The method is based on the persistent scatterer interferometry (PSI) technique in order to detect newly constructed buildings and estimate their heights in a selected case study area in Athens, Greece. The overall objective is to derive timely spatial information for building activity. A key concept of the approach is the residual height, i.e., the difference in height of each point compared to a reference point that is suitably selected. The data used are acquired by the Sentinel-1 satellite. Both ascending and descending orbits and dual polarizations (VV/VH) are used. The results show that as much as 70% of new buildings can be detected at a vertical accuracy approximately of 2.5 m, which is sufficient to determine the number of stories per building. Overall, the proposed method can provide an efficient insight regarding building activity and provide a significant information layer for urban studies in a rapidly changing world.

Keywords: persistent scatterer interferometry; synthetic aperture radar; change detection; urban areas; building extraction; building heights

check for updates

Citation: Letsios, V.; Faraslis, I.; Stathakis, D. Monitoring Building Activity by Persistent Scatterer Interferometry. *Remote Sens.* **2023**, *15*, 950. https://doi.org/10.3390/rs15040950

Academic Editors: Georgia Koukiou and Vassilis Anastassopoulos

Received: 16 December 2022
Revised: 5 February 2023
Accepted: 6 February 2023
Published: 9 February 2023

Copyright: © 2023 by the authors. Licensee MDPI, Basel, Switzerland. This article is an open access article distributed under the terms and conditions of the Creative Commons Attribution (CC BY) license (https://creativecommons.org/licenses/by/4.0/).

1. Introduction

Constructions as a sector of the economy amounts to a significant part of the gross domestic product (GDP) in any country [1]. Construction stimulates the economy as it directly and indirectly sustains employment. Conversely, when the economy is not doing well, a reduced number of new buildings is expected. Therefore, the volume of construction can largely vary through time, especially when the economy is not stable. A typical example is Greece during the past decade. The debt crisis that the country faced starting in 2008 and the subsequent austerity measures heavily affected constructions, eventually bringing new building activity practically to a complete standstill. Recently however, the economic climate has improved and a substantial boost in the construction sector is noticeable in most Greek urban areas and in some touristic destinations. Currently a new building activity trend is starting to emerge. The impact of the emerging energy crisis drives the prices of construction materials to unprecedented levels and makes potential home buyers more inclined towards postponing spending. The official data clearly highlight the substantial drop in new building permits during the economic recession period. Despite the rebound in recent years, even today the number of permits is less than half compared to the 2008 level. The evolution of new building permits during this period, as captured by the Hellenic Statistical Authority, is shown in Figure 1. Remarkably, in 2008 the number of permits was 66,740, whereas in 2021 it was 23,807.

While building permit statistics does provide a broad picture of the evolution of new buildings, this picture is far from perfect. First, it is unclear whether all permits eventually materialized in actual buildings. Second, there is a time lag between obtaining the permit

and actually constructing the building. By law, each permit is allowed an implementation period of four years plus two years of possible extension. Therefore, the exact date of construction can follow the date of the permit for as much as six years in total. There is no way to determine the actual construction date (if constructed) within this time-frame. Also, the spatial resolution that official statistics provide is relatively coarse. The data are aggregated at the municipality level. Hence, there is no clear spatial dimension to evaluate which actual areas within the cities attract the most pressure for new buildings. The exact locations and heights do not become available as public domain data.

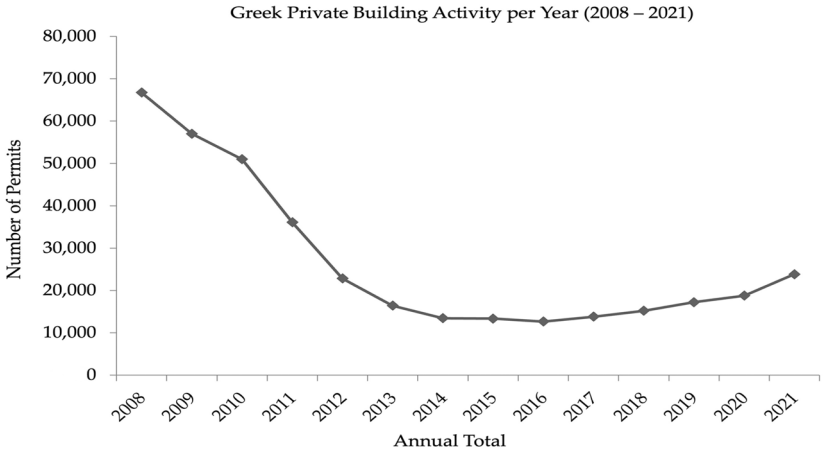


Figure 1. Graphical representation of the annual private building activity.

Another major problem with official statistics is that only legal activity (permits) is recorded. Undoubtedly however, illegal building activity is an existing long-term problem in many countries that cannot be neglected.

Illegal building generates a de facto situation that reduces the degrees of freedom available to urban planners. Land use, planning for open spaces, environmental protection, infrastructure provision (water, transportation etc.), urban resilience to natural disasters, all become more difficult to manage. An assessment of actual built space ("as-built") is essential in order to estimate the pressure imposed on urban areas. Accurate and timely knowledge is essential also for monitoring urban sprawl which is a major driver of environmental degradation in many types of urban space [2–4].

It is a fact that in recent decades, efforts to curtail illegal constructions have intensified. These efforts have been coupled by measures to legalize existing illegal structures as a more socially and economically acceptable alternative to demolishing tens of thousands of them. Based on official data provided by the Technical Chamber of Greece, in the last decade 2010–2020, slightly more than 1.5 million applications were made for the legalization of structures. Among them, 25% (550,000) correspond to buildings that totally lack permits.

It is well understood that the urban space is complex and consists of diverse structures and networks. This heterogeneity substantially increases the difficulty of studying and monitoring urban areas. Traditional optical remote sensing is suitable for monitoring built-up changes horizontally, in two dimensions [5–8].

However, monitoring changes vertically, i.e., focusing on the changes in the height of buildings, is much more cumbersome when relying solely on optical remote sensing. Recently however, a promising alternative has emerged that is based on very high resolution (VHR) radar data and a technique known as interferometry. Synthetic aperture radar (SAR) interferometry is now a well-known remote sensing technique that takes advantage of the phase difference between two SAR images and can precisely express it in the height or deformation values of each physical or artificial target on the earth's surface. To overcome limitations of basic interferometry (geometric, temporal, and atmospheric decorrelations), persistent scatterer interferometry (PSI) was introduced [9]. PSI uses long-time series of

images (e.g., more than twenty) to locate permanently stable reflectors (persistent scatterers) in time. This results in a very high accuracy of measurements.

Several approaches for built-up area detection, building change detection, building footprint extraction, and urban target recognition have emerged. In Ref [10], an approach for built-up mapping using time series from Sentinel-1 radar data is presented, using both ascending and descending orbits, based on the fact that buildings reflect radiation highly and coherently over time. In Ref [11], the fact that artificial objects such as buildings appear very bright and stable in SAR images was exploited, and a coherence change detection method was applied in a time-series of Sentinel-1 SAR images to monitor urban growth and damage detection over urban areas. In Ref [12] a method is presented for mapping built-up space with the use of Sentinel-1 SAR data. The method is based on the change presented by the built-up space, on the change in brightness in a radar image due to shadows and the double-bounce effect, and their spatial correlation. In Ref [13] high-resolution multi-temporal TerraSAR-X images were used for built-up change detection and monitoring. The method takes advantage of the PSI technique and a change detection procedure that recognizes disappearing big-chance and emerging big-chance points, along with their occurrence times.

Change detection for buildings has also been proposed based on SAR data and deep learning networks [14–17]. In Ref [18], a building detection method is proposed based on extracting dark and bright regions from a SAR image and combining them with the given shadow direction to detect the buildings. In [18] an unsupervised approach is proposed based on using multi-temporal fully polarized SAR images to highlight constructed and demolished built-up elements. In Ref [19], a unified framework for building segmentation in SAR images is proposed. In Ref [20], a block-diagonality test statistic for reflection symmetry is introduced, with a constant false alarm rate property for quad-polarimetric SAR data in order to detect artificial structures. In Ref [21] a novel method for building detection is proposed, using repeat-pass E-SAR satellite full-polarimetric data in L-band with a one-day temporal difference (baseline). The authors of [22] used multi-temporal VHR SAR images over two urban areas in Italy to detect new or fully demolished buildings based on information extraction due to changes in backscattering at the optimal building scale and the exploitation of the expected backscattering properties of buildings to detect either new or fully demolished buildings.

The authors of [23] introduced a method of fusing dual-aspect SAR images aiming to extract building footprints based on VHR (1 m) SAR images. Due to the side-looking mechanism of the SAR system, buildings usually present a bright line feature called an L-shape. Footprint extraction is possible based on the combination of ascending and descending orbits. High accuracy building footprint extraction is also possible by combining geometry and a set of features evident in buildings (double-bounce, layover, shadow) in a single VHR SAR radar image [24]. In Ref [25] it was assumed that built-up areas appear brighter in a SAR image than other land covers due to the very high backscatter energy and buildings being very stable in time, and used machine learning on dual-polarization Sentinel-1 images to detect building footprints. In Ref [26], a method was developed for detecting the number of buildings in a single VHR radar image. The authors of [27] used a method based on the interferometric coherence between radar images and the study of some local area statistics, such as the speckle divergence index and the difference between the mean and median coefficients of the reflected electromagnetic radiation for building detection using Sentinel-1 SAR data.

In Ref [28] a method is introduced for urban target recognition using a long-time series of ERS and Envisat radar images over Milan in Italy. Based on the physical nature of persistent scatterer targets, it was possible to measure a set of features including building height, deformation trend, and the birth and death date of a persistent scatterer point and the temporal coherence. Based on these features, urban targets such as roofs and poles can be classified.

It is evident that a method to record building activity in three dimensions (location and height) at a fine spatial and temporal resolution is desirable, given the lack of suitable official statistics. An annual layer that has per-building information is a valid objective. Such an information layer is useful for many urban and socioeconomic applications. The PSI technique using dual-polarizations and both orbits (ascending/descending) of the Sentinel-1 satellite is an appealing option to construct this information layer. A central concept of the proposed approach is the "residual height" or "residual topographic error (RTE)" which results after subtracting the topographic phase component using an external digital surface model [29]. Since the PSI technique aims to calculate the height and deformation of each PS with respect to a reference point, the "residual height" actually refers to the height difference between the reference and all other PS points. In effect, the residual height states how much higher or lower each point is compared to the reference. The idea is that by selecting a low-rise building as the reference point, all higher points probably correspond to buildings. The proposed method was implemented to identify newly constructed buildings and estimate their heights for the time period from the beginning of 2018 to the end of 2021. The data and study area are presented in Section 2, the method is then explained in detail in Section 3, and the results are shown in Section 4.

2. Materials and Methods

2.1. Study Area

One municipality of Athens (namely, Papagos-Cholargos) is selected as the study area. The study area is a suburb located approximately eight kilometers northeast from the city center and covers an overall area of 7.41 square kilometers, as shown in Figure 2.

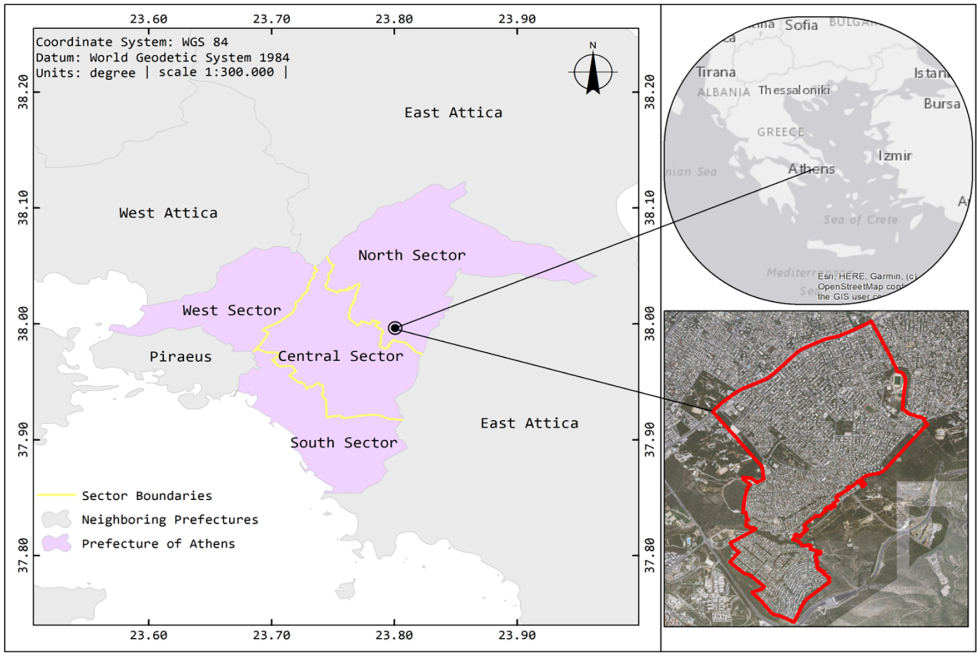


Figure 2. Study Area.

The main reasons for selecting this area are that it characterized by a clear layout, almost all the land parcels are of comparable in size (400–500 m^2), and the maximum allowed building height is relatively stable throughout the area (18 m.). It is worth mentioning that a typical story height in the area is approximately 3.3 m. Therefore the maximum allowed high typically translates into five floors (ground floor plus four). The main construction material is reinforced concrete and the building covering is a tiled roof or a terrace. During the past two to three years, the area is facing intense construction activity following a decade of a complete stand-still.

2.2. Data

The data used in this research are SAR SLC-IW dual-polarization images acquired by the Sentinel-1 satellite, collected through the Alaska Vertex Hub (https://search.asf.alaska.edu, accessed on 10 May 2022). A total of 346 images were collected from both orbits and both available polarizations of this satellite were utilized, as shown in Table 1.

Table 1. Data description.

Parameters	Ascending	Descending
Satellite Sensor	Sentinel-1A	Sentinel-1A
Number of Images	159	187
Orbit	102	109
Swath and Polarization	2 VV/VH	3 VV/VH
Sensing Period	5.1.2017/7.8.2022	11.5.2016/27.7.2022
Rg × Az Resolution	2.33 × 13.93 m.	2.33 × 13.90 m.
Wavelength (λ)	5.55 cm.	5.55 cm
PRF (Hz)	1717.13	1717.13
Range Bandwidth (MHz)	56.5	56.5
Azimuth Bandwidth (Hz)	327.0	327.0
Master Image	25 April 2019	13 June 2019
Incidence Angle (study area)	39°	45°
Temporal Baseline (days)	12	12
Average Normal Baseline	−135.28 m.	−103.20 m.

As already mentioned in Section 1, the residual height parameter plays a key role in this research. Since we are focusing on buildings, it was indispensable to create a high-resolution auxiliary DSM by the processing of Level 1-B cloud-free Pleiades tri-stereo images acquired in 2016 with an RMSE of 1.17 m [30].

2.3. Method

This section is divided into three sub-sections, consisting of preprocessing, atmospheric phase screen estimation and new building detection, and height estimation. Figure 3 shows the general flowchart of the proposed method.

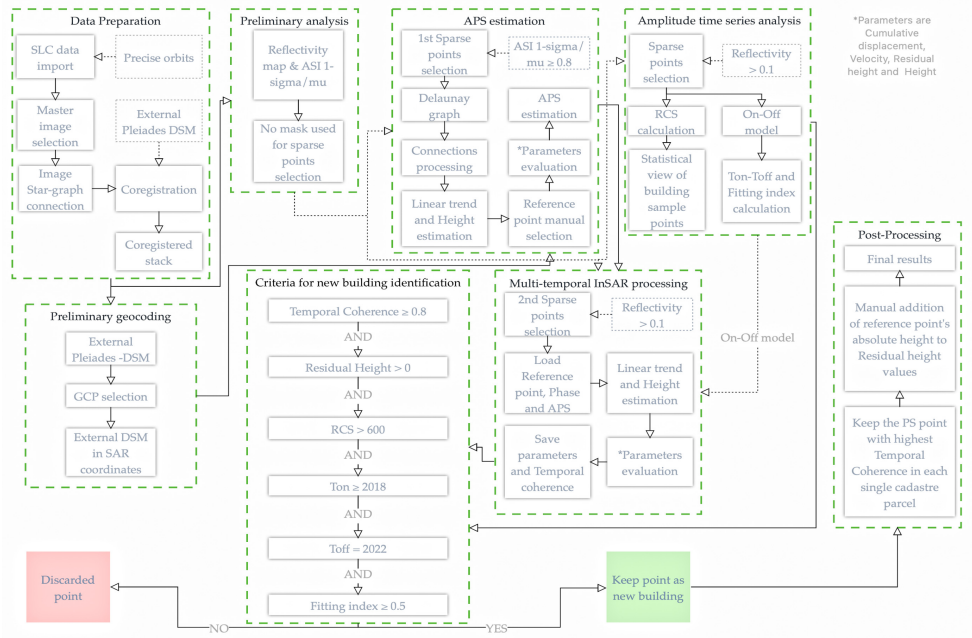


Figure 3. Flowchart of the proposed method.

2.3.1. Preprocessing

The first step in the PSI technique is to select the connections between the images. As the focus is on buildings, which exhibit high coherence over time, the single "master" approach is adequate. All "slave" images are connected to the same common master image that constitutes the principal graph of the PSI. The selection of a master image in both orbits is made, taking into account the barycenter to be as close as possible to the center of the time series and, at the same time, to achieve large normal baselines (i.e., the distance between two different satellite observations over the same area) which is the tricky part of working with Sentinel-1 SAR data. The orbit files contain information about the exact position of the satellite and are very important for an accurate coregistration between the images. Figures 4 and 5 illustrate information from both ascending and descending datasets.

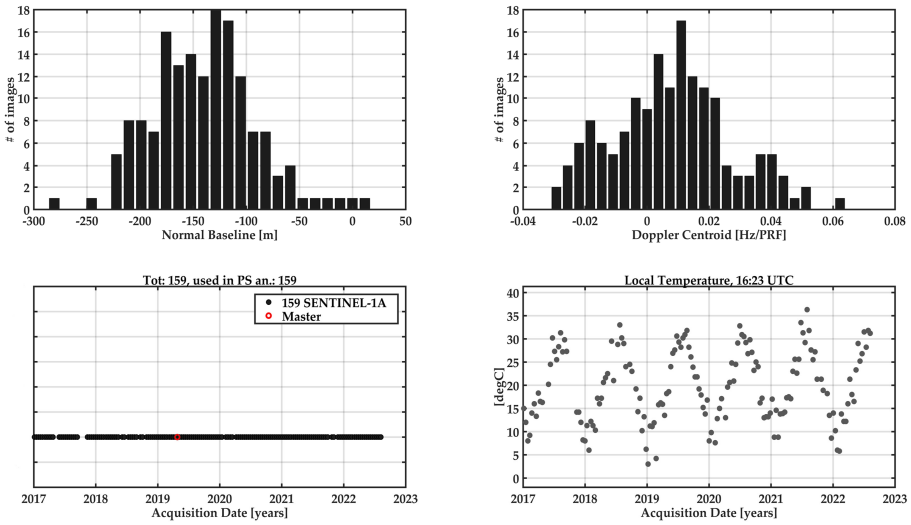


Figure 4. Dataset of the Ascending Orbit. The **upper left** graph illustrates the normal baseline distribution of image pairs. The **upper right** graph illustrates the Doppler centroid distribution of image pairs. The **lower left** graph illustrates the acquisition date range of the data time series. The **lower right** graph illustrates the local temperature per acquisition date.

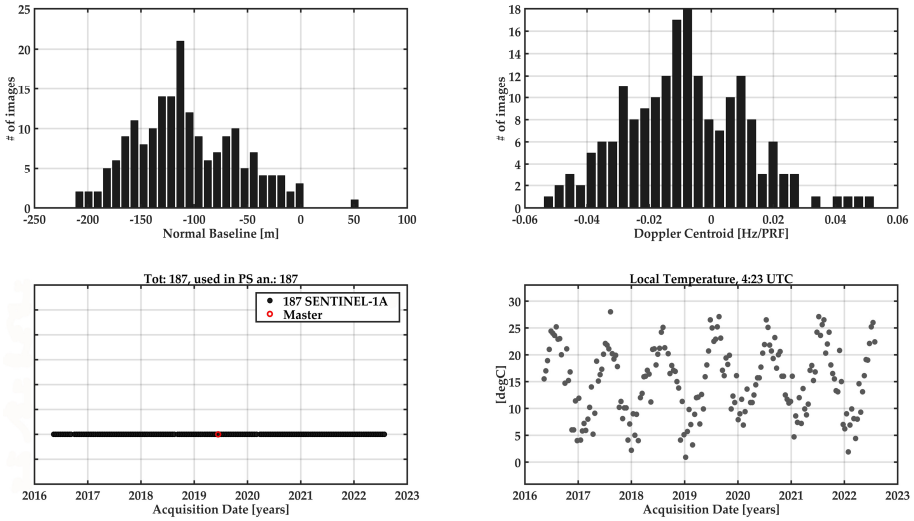


Figure 5. Dataset of the Descending Orbit. The **upper left** graph illustrates the normal baseline distribution of image pairs. The **upper right** graph illustrates the Doppler centroid distribution of image pairs. The **lower left** graph illustrates the temporal baseline. The **lower right** graph illustrates the local temperature per acquisition date.

With the completion of the coregistration, the next step is the creation of the "reflectivity map" and the amplitude stability index 1-sigma/mu (ASI 1-sigma/mu), as illustrated in Figure 6.

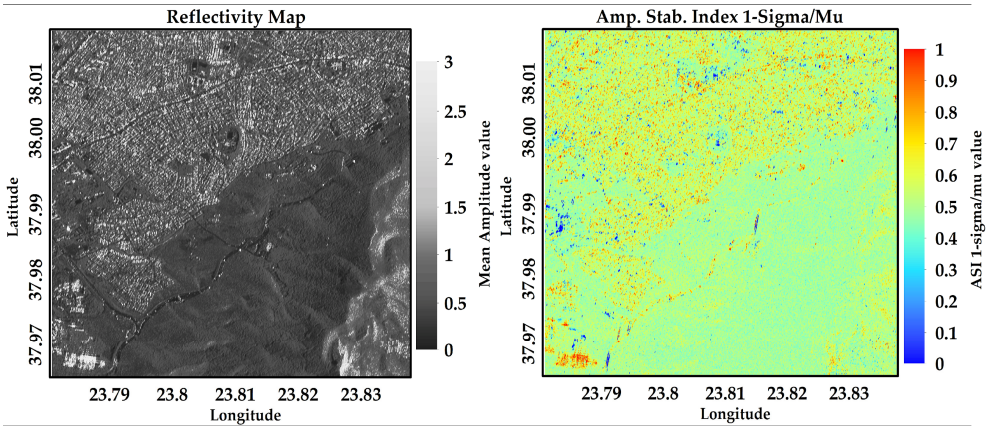


Figure 6. Geocoded Reflectivity Map on the **left** and geocoded ASI 1-sigma/mu on the **right** (example of Descending VV data).

The reflectivity map is the display of the average value of the amplitude for each pixel. The ASI 1-sigma/mu is an amplitude-based index and shows the amplitude dispersion of each pixel. The usage of this indicator refers to the selection of PS candidates (PSC) assuming that points with stable amplitude values present small phase dispersion. The authors of [9] introduced the dispersion index D_A (1), suggesting a suitable threshold for the first selection of PS points $D_A < 0.25$.

$$D_A = \sigma_A / m_A, \quad (1)$$

where m_A and σ_A are the mean and the standard deviation of the amplitude values. By reconstructing (1) to set the measurement of the index on a scale from 0 to 1, Equation (2) was obtained.

$$\text{ASI 1-sigma/mu} = 1 - D_A = 1 - \sigma_A / m_A, \quad (2)$$

The PSI technique searches for a persistent scatterer point in each pixel individually. It has been proposed that selecting the points which correspond to the main lobe of the cardinal sine by creating a mask based on the local maxima is more efficient [31]. As electromagnetic radiation travels both ways, from the satellite to the target and from the target back to the satellite in a continuous wave, cardinal sine is the cross-correlation between transmitted and received radiation and represents the actual signal measurement. The cardinal sine corresponds to the resolution of the system and is inversely proportional to the bandwidth. It was found in this study that relying solely on cardinal sines results in information loss. For that reason, all points were used instead. Furthermore the ground control points (GCPs) were selected to be clearly visible in the SAR images as points of significant electromagnetic radiation backscattering. The final stage of preprocessing is the transfer of the auxiliary DEM to the satellite reference system (SAR coordinates) to be used during the PSI processing.

2.3.2. Atmospheric Phase Screen (APS)

Repeat-pass SAR interferometry suffers from atmospheric variations that affect the transmitted signal of the satellite and degrade the final measurements by contributing to the phase difference. To remove it, an atmospheric phase screen procedure is based on the general rule that the atmosphere changes rapidly in time but not in space. For example, the atmospheric effect between two adjacent points (e.g., that are a few hundred meters apart) is too small to impact the phase difference between them. Applying this rule in a larger study area, a triangulation network must be set between stable points aiming to

measure the height (Δh) and velocity (Δv) differences between connections, as represented in Figure 7.

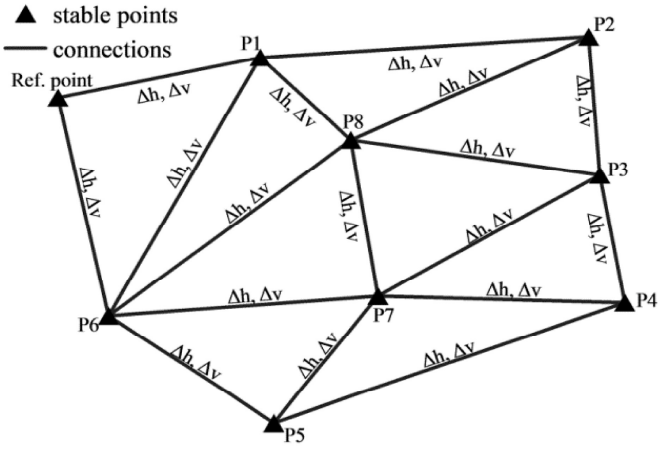


Figure 7. Triangulation network between stable points for atmospheric phase screen calculation.

The differences are integrated across the graph in order to calculate the height and displacement values of each node. It was chosen here to connect points with ASI 1-sigma/mu $\geq$0.8, based on the assumption that this value indicates points that are stable enough in time. Figure 8 illustrates the triangulation network based on the selected persistent scatterer candidate points (PSC).

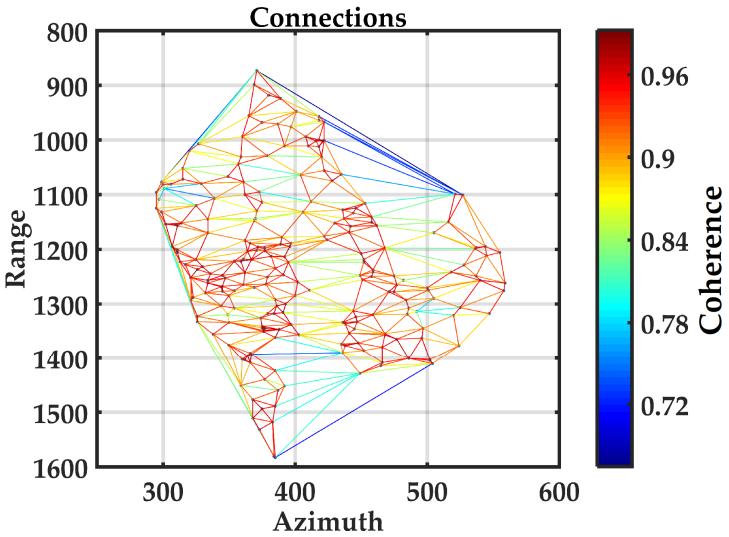


Figure 8. Triangulation network between the selected PSC points. The color lines represent the coherence of each connection between two close PSC points. Connections presenting coherence equal to or higher than 0.7 were used (example of descending VV data).

The PSI technique calculates the height and displacement always relative to a fixed reference point that needs to be defined. This point was set on the roof of a two-story school in the area that appears as a very distinct target and can be easily detected in the SAR images with ASI 1-sigma/mu = 0.8 and temporal coherence = 0.94.

To assess the quality of the model, the histograms representing the distributions of height difference (m.) and displacement velocity (mm/year) relative to the reference point are shown in Figure 9.

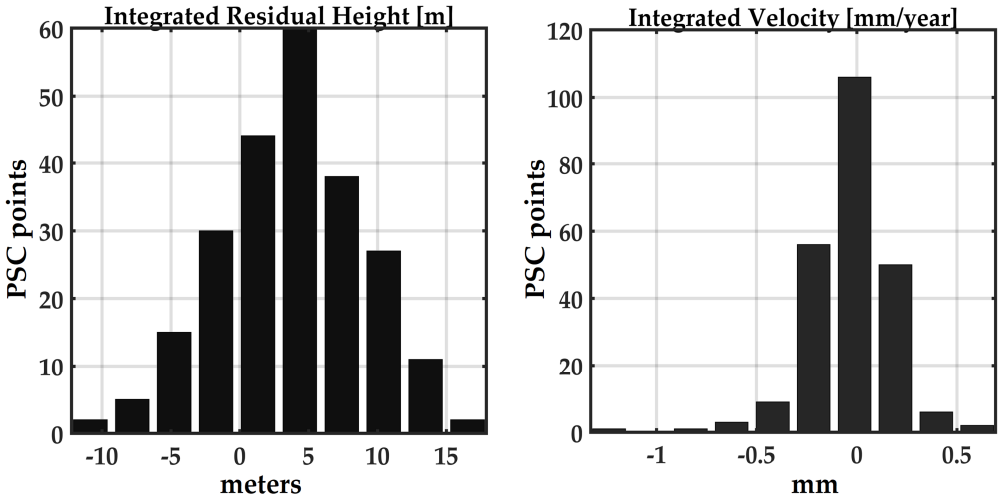


Figure 9. Estimated residual height histogram (**left**) and estimated velocity histogram (**right**) during APS calculation. Histograms represent the distribution of the integrated residual height and integrated velocity for each point with respect to the reference point (example of descending VV data).

It is evident in this figure that the residual height observed conforms with the expected values based on the maximum allowed building height, and also that the points are stable (zero velocity), and by extension the reference point too. Figure 10 shows the temporal coherence of PS points after removing the estimated APS.

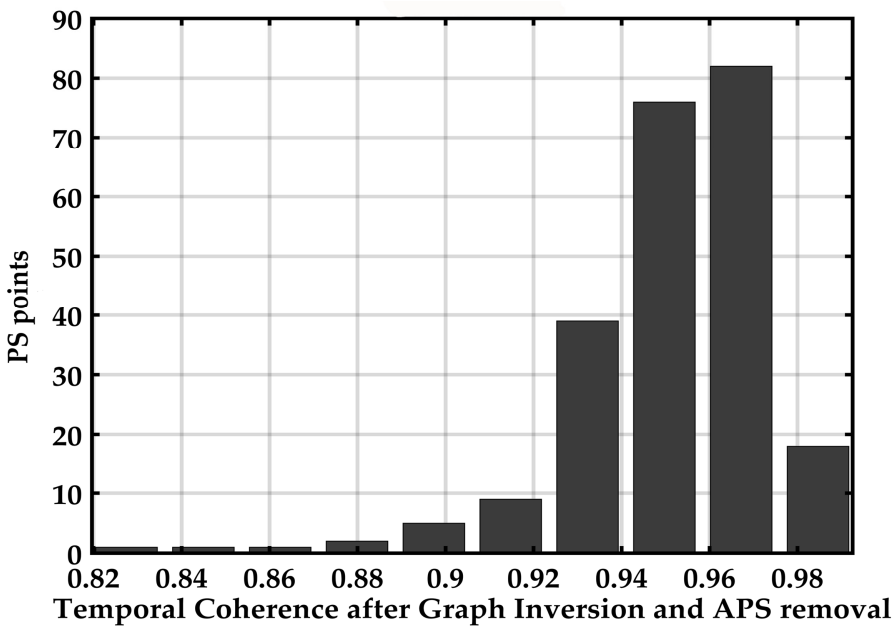


Figure 10. Temporal coherence histogram after atmospheric phase screen removal (example of descending VV data).

Given that optimal coherence yields a value of one, it is evident that an accurate model, and thus reliable measurements, has been achieved. Figure 11 shows an example of a flattened and DEM removal interferogram before and after APS estimation. The comparison between elements (a) and (b) highlights the APS contribution which reconstructed the original interferogram in a smoother version free of atmospheric noise.

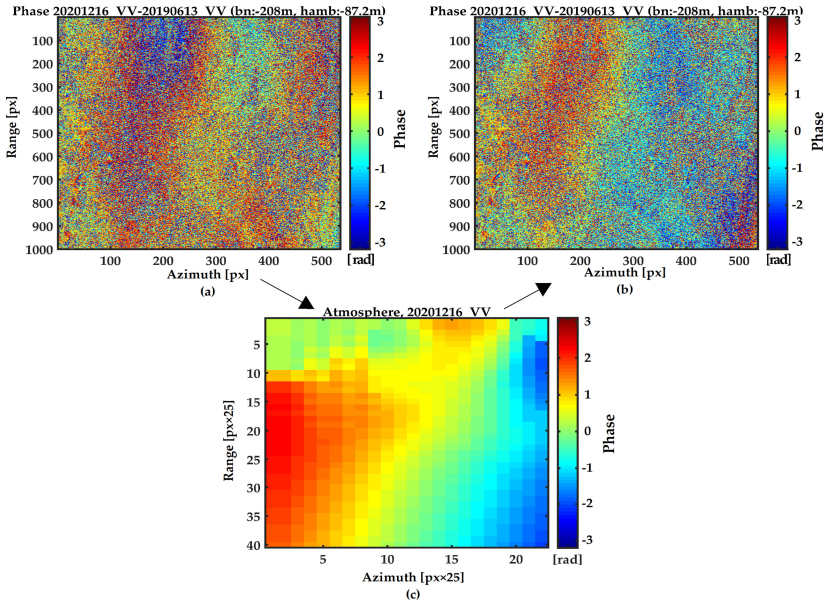


Figure 11. Example of APS contribution in the interferometric phase. Element (**a**) shows the interferogram before APS estimation, while (**b**) shows the same interferogram after APS estimation and element (**c**) shows the calculated atmosphere. B_n refers to the normal baseline and h_{amb} refers to height of ambiguity (example of VV-descending data). A standard evaluation of the atmosphere is the nonappearance of big "phase jumps" that indicates the good quality of the APS estimation.

2.3.3. New Building Identification and Height Estimation

Multi-temporal PSI analysis was applied to pixels showing reflectivity values higher than 0.1, assuming that almost all points in the study area will be included as PSC in parameters calculation. The selection of this low value derives from the assumption that some PSC points may present low reflectivity and ASI 1-sigma/mu values due to their birth date that differs from the beginning of the data time series. In a nutshell, selecting PSC points based on a standard method, such as a moderate dispersion index value, may cause the loss of pixels which are candidates to classify as new buildings. In conjunction with the on-off model as weight in the multi-temporal analysis, as stated below, the temporal coherence will be the factor to clarify which of them constitute PS points. The proposed method emphasizes the key role of the residual height parameter in combination with some other metrics, since the assumption is made that objects higher than the reference point are buildings. The parameters in specific are the Ton/Toff values derived by the amplitude time series analysis and the fitting index, the temporal coherence, the residual height, and the radar cross section (RCS).

The on–off model accompanied by the fitting index adapted in SARPROZ software (8 September 2022 version) was used for the amplitude time series analysis and the T_{on} (birth) and T_{off} (death) dates estimation. Abrupt changes in amplitude values with respect to time are detected based on a Bayesian change-point step detector algorithm [32]. The model analyses the amplitude as a function of normal baseline, Doppler centroid, temporal baseline, and temperature, which constitute the characteristics (Θ_{amp}) of a hypothetical target k [33,34]. The fitting index (ξ_{amp}) (3) represents the degree of agreement between the model and the data measuring on a scale from 0 to 1, and can consider as an amplitude stability advance measure [28].

$$\xi_{amp,k} = 1 - \frac{\sum_i |\alpha_{i,k}^{rec} - a_i\left(\Theta_{amp,k}\right)|}{\sum_i |a_{i,k}^{rec}|} \quad (3)$$

where $\alpha_{i,k}^{rec}$ are the received amplitude data, α_i are the model values as a function of target characteristics. In the data time-series some points start functioning as persistent scatterers

right from the beginning (t_0), whereas others start later within the observed period (t_n). These times are the basis on which to identify the newly constructed buildings. Typically, when studying a time series in urban areas, several patterns are identified as described in Table 2.

Table 2. Typical patterns in urban areas.

Pattern	T_{on}	T_{off}
demolition	$t = t_0$	$t < t_n$
ephemeral	$t > t_0$	$t < t_n$
new building	$t > t_0$	$t = t_n$
persistent scatterer	$t = t_0$	$t = t_n$

The detection of a new building is based on the concept that its corresponding persistent scatterer points initially do not exist in the time series. They emerge later ($T_{on} > t_0$) and they remain apparent until the end of the time-series ($T_{off} = t_n$). This pattern is graphically displayed in Figure 12c in juxtaposition with the other alternative patterns.

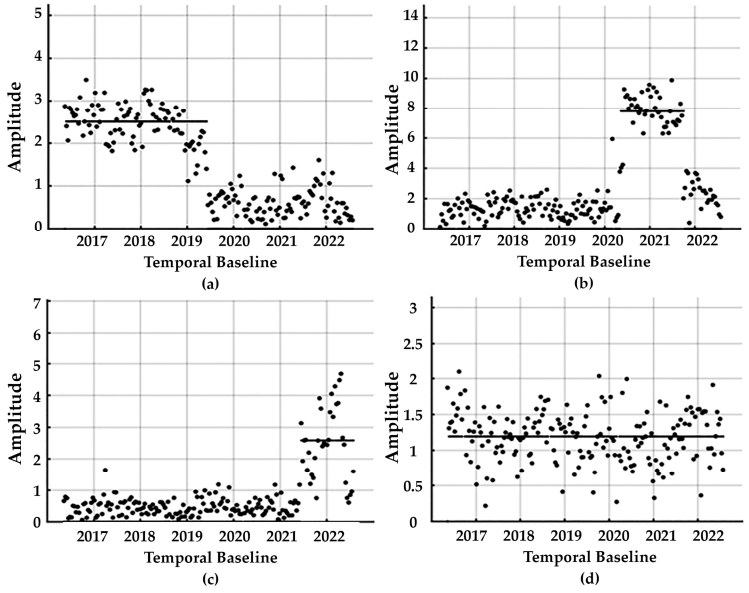


Figure 12. Illustration of the different patterns present in the time-series named in Table 2 as (**a**) demolition, (**b**) ephemeral, (**c**) new building, and (**d**) persistent scatterer.

It must be noted that the on–off model was used as a weight (w_i) during the multi-temporal PSI analysis. The weight (w_i) acts as a flag that defines which subset of interferograms related to birth and death dates the method must consider calculating the parameters. The weighted PSI approach introduced in [35], and the utilization of weights, can be implemented with a modification of Equation (4) that leads to Equation (5).

The maximum of the absolute value of the periodogram is called temporal coherence (4) and is the indicator that separates whether a point operates as PS or not [36].

$$\gamma\left(\Delta_h, \Delta_v\right) = \frac{1}{N}\sum_{i=1}^{N} e^{j\left(\Delta\varphi_{obs} - \frac{4\pi}{\lambda}\frac{B_{n,i}}{R}\frac{\Delta_h}{\sin\theta} - \frac{4\pi}{\lambda}B_{t,i}\,\Delta_v\right)}, \tag{4}$$

where γ refers to temporal coherence, height (Δ_h) and velocity (Δ_v) are the unknowns of each point to be estimated, N refers to the interferometric pairs, $\Delta\varphi_{obs}$ is the observed phase, B_n is the normal baseline, B_t is the temporal baseline, R is the sensor-to-target distance, θ is the incidence angle, and λ is the sensor wavelength.

$$\gamma\left(\Delta_h, \Delta_v\right) = \frac{1}{\sum w_i}\sum_{i=1}^{N} w_i e^{j\left(\Delta\varphi_{obs} - \frac{4\pi}{\lambda}\frac{B_{n,i}}{R}\frac{\Delta_h}{\sin\theta} - \frac{4\pi}{\lambda}B_{t,i}\,\Delta_v\right)}, \tag{5}$$

where all parameters are the same as Equation (4) and the w_i is the imported weight.

In the subsequent analysis, points with temporal coherence values equal to or higher than 0.8 are selected, indicating good quality as persistent scatterers to reliably estimate the height difference measurement related to the reference. Figure 13 illustrates PS point parameters.

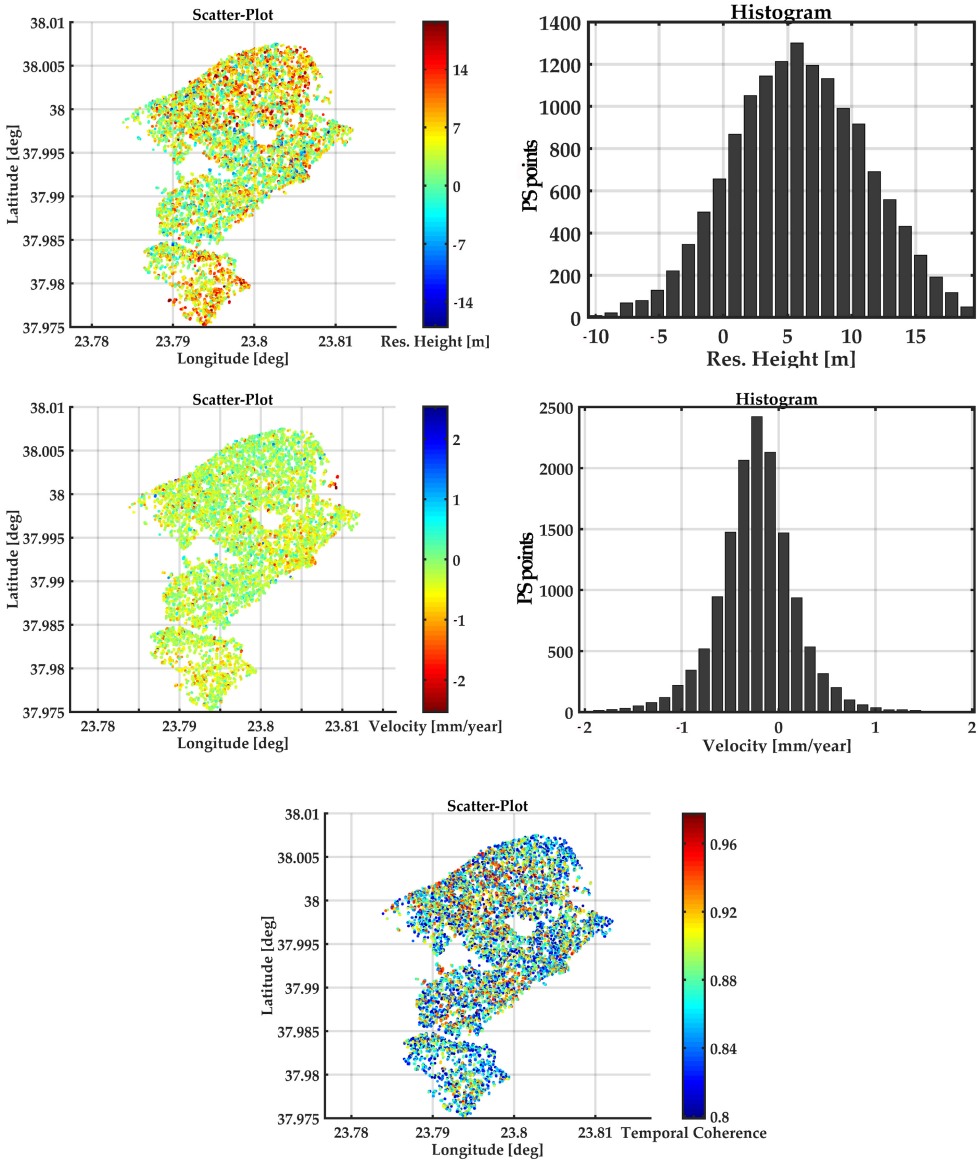


Figure 13. The top is the residual height map with the histogram, on the middle is the deformation velocity map with the histogram and the bottom is the temporal coherence map.

From the residual height histogram shown in Figure 13, the values are concentrated around the value of five meters, which is reasonable considering the characteristics of the reference point and the study area.

Accordingly, the velocity histogram is reasonable given that values are centered around zero, indicating a stable area.

The relative building heights are recorded in relation to the reference point. To obtain the absolute heights, the reference height has to be added. The height of the reference point was calculated at 6 m from the ground level based on the DSM.

The radar cross section (RCS) is a measure of signal reflection, i.e., how detectable each ground target is by the radar [28]. It calculates the electromagnetic cross-sectional area in which the echoes of the reflected signal are dispersed, and is symbolized by the letter σ. The unit of measurement is square meters. It depends on the physical size of the target, the

shape, the direction of the target to the satellite, the construction material, the incidence angle of the electromagnetic radiation, polarization, and the reflection mechanisms of the targets. It is defined as the physical size of a hypothetical uniform sphere that has a radar cross section equal to the value of the intensity of the reflected signal.

It is worth mentioning that RCS calculation using SARPROZ is based on data calibration with the use of ERS SAR images and corner reflectors over the urban area of Milan, Italy [28]. We believe that due to the similarities between ERS and Sentinel-1 satellites, the RCS is usable as a reference even if it is not calibrated with our data.

Table 3 shows the statistical view of the RCS based on the selected sample of PS points with temporal coherence >0.8, ASI 1-sigma/mu > 0.7, and falls within the building footprints that were available as an auxiliary shapefile.

Table 3. Descriptive statistics of radar cross section (RCS) building sample (example based on VV/descending data).

Descriptive Statistics	
Mean	1627.96
Median	1148.36
Standard Deviation	1746.37
Kurtosis	59.99
Skewness	6.23
Min	625.12
Max	28,568.71
Sample Population (PS points)	1783

The above processing steps were performed four times to extract results from all polarizations and orbits (ascending VV/VH, descending VV/VH). The set criteria are used in order to identify the newly constructed buildings in the study area and estimate their height. The specific thresholds used to classify persistent scatterer points as buildings are displayed in Table 4.

Table 4. The proposed criteria aim to highlight newly constructed buildings.

Criteria for New Building Identification	
1.	Ton $\geq$ 2018
2.	Toff = 2022
3.	Temporal Coherence $\geq$ 0.8
4.	Residual Height > 0
5.	Radar Cross Section (RCS) > 600
6.	Fitting Index $\geq$ 0.5

In a nutshell, new buildings are points that emerged during or after 2018 and remained until 2022, with high temporal coherence values to ensure that the points actually function as persistent scatterers, higher than the reference point (i.e., higher than the low-rise building that was selected as a reference), and with a significant radar cross section value so that smaller targets that meet the criteria (poles, solar water heaters, small metal structures at the building rooftops, etc.) are not mistaken.

Inevitably, sometimes more than one persistent scatterer point appears over a newly constructed building, as shown in Figure 14. This may be due to the point being detected in more than one orbit and polarization or because of the object size, since we are not working with cardinal sines. To limit the effect of this problem, an auxiliary vector cadaster polygon file was used and only the point in each land parcel that presents the highest temporal coherence (higher accuracy) was maintained. Due to planning restrictions and plot sizes in this study area, it is highly unlikely that a second building exists in the same plot.



Figure 14. Example of more than one PS point appearing over each newly constructed building. Polygons refer cadastral land parcels.

3. Results

The results of the proposed method include three aspects of detecting new buildings: the location of new buildings, their construction date, and their height. Based on the proposed method, 59 new candidate properties that may present building changes have been identified as shown in Figure 15. Their basic statistics per classification criterion are shown in Table 5.

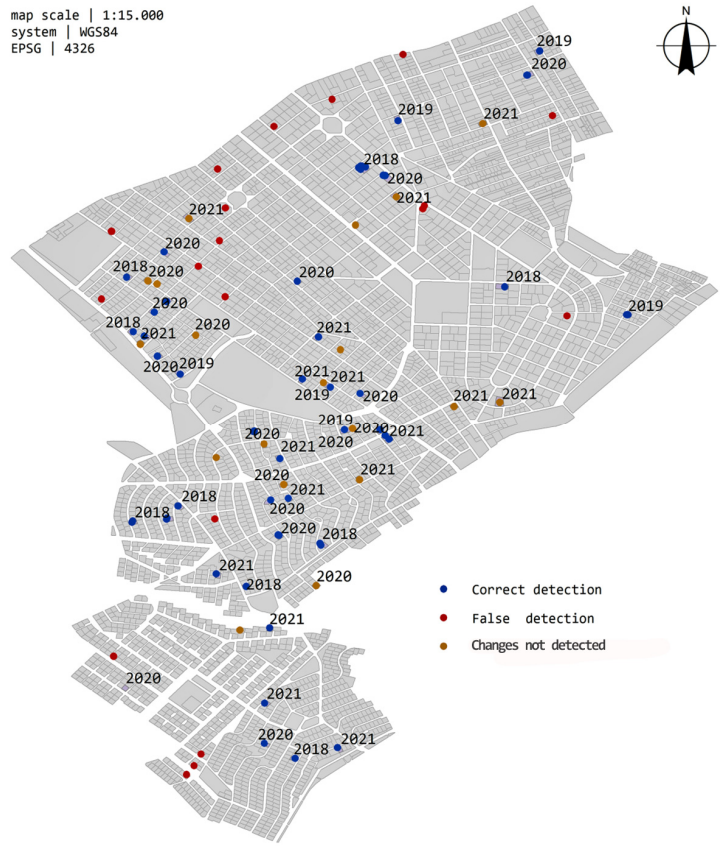


Figure 15. Visualization of detected PS points that may represent newly constructed buildings. Blue color corresponds to the correct detection of the method accompanied by date of construction, red corresponds to false detection and orange corresponds to real new buildings accompanied by date of construction that the method failed to detect.

Table 5. Classification criteria statistics.

	Fitting Index	Temporal Coherence	RCS (m^2)	Reflectivity	ASI 1-Sigma/mu	Residual Height
Average	0.57	0.89	3657.91	1.75	0.25	7.20
Min	0.50	0.81	727.08	0.70	0.04	1.53
Max	0.75	0.98	24,524.83	4.02	0.56	12.93

To validate the results, several open databases were used to determine the actual construction date and height of buildings. For construction dates, the Google Earth Pro platform, which offers a historical archive of very high-resolution images with a refresh rate of up to three images per year, was used. Also, building permits that are available online since 2019 were used for building heights and locations (https://apps.tee.gr/adeiapublic/faces/main, accessed on 8 June 2022). To determine the heights before 2019 the portal Mapillary (https://www.mapillary.com/, accessed on 8 June 2022) was used, which provides street-view photos. Based on the validation datasets, the actual total amount of newly constructed buildings in the study area is 56. The location validation for the results of the proposed method showed that forty of them were predicted correctly as shown in the accuracy matrix in Table 6.

Table 6. Commission and Omission Errors.

Detected Properties Population [1]	Ground-Truth Data Population	Correct Prediction	Commission Error	Omission Error	Accuracy Rate [1]	Accuracy Rate [2]
59	56	40	19	16	67.80%	71.43%

Commission error is the comparison between the detected candidate new buildings and the number of correctly identified ones accompanied by Accuracy Rate [1]. The omission is the comparison between the correctly identified new buildings vs the actual changes that were collected as ground-truth data accompanied by Accuracy Rate [2].

The construction date validation shows that the method is very accurate; in all cases, detection is possible within eight months from construction. The height validation shows that the 40 buildings we identified and correspond to real changes represent an efficient accuracy as described in Table 7, considering that in Greece a typical floor-to-floor height in buildings is approximately 3.3 m.

Table 7. Verification of calculated building heights.

Descriptive Statistics (Meters)	
Mean Absolute Error (MAE)	2.35
Standard Deviation	1.00
Median	2.51
Min	0.47
Max	3.94
RMSE	2.55
RMSE 95%	2.24

4. Discussion

The primary goal was to detect new buildings. The results show that most, but not all, new buildings are detected by the proposed method. The method is not able to detect some new buildings. The omission errors are due to a residual height value that does not pass the set threshold. This can happen because the scattering center of the target, which is generally unknown, can be low in the building facade. In some other cases, a low-rise building pre-existed and a few stories were added on top of it. As a result, abrupt changes in the reflectivity value do not appear. In other instances, due to the satellite resolution and the object's orientation, the method cannot distinguish between two adjoining attached

buildings. This finding indicates that the method's efficiency is reduced by using moderate resolution Sentinel-1 data, for areas that present an attached planning system, and the objective is per-building detection. The commission errors, the incorrectly detected points as new buildings, are mainly due to mistaken reflectivity changes. It is known that SAR images before co-registration are not perfectly aligned and present pixel offsets. The combination of the moderate resolution imagery used and the different speckle noise of each image probably generates this false alarm for abrupt changes in the reflectivity in some situations.

The secondary goal was to estimate the heights of the new buildings. The verification result was sufficient since the MAE was equal to 2.35 m and the RMSE equal to 2.55 m, highlighting the high potential of the PSI technique for such applications even with the use of moderate resolution data. The disadvantage concerning height calculation with the use of Sentinel-1 compared to other SAR satellites with similar resolution and wavelength derives from the small normal baselines that Sentinel-1 usually presents. The larger the dispersion of the normal baselines, the smaller the variance of the estimated heights [36]. Equation (6) states that claim.

$$\sigma_{\Delta h}^2 = \left(\frac{\lambda R \sin\theta}{4\pi}\right)^2 \frac{\sigma_{\Delta\varphi}^2}{N\sigma_{Bn}^2}, \quad (6)$$

where Δh is the height, $\Delta\varphi$ is the observation phase, Bn is the normal baseline and λ, θ, R are the sensor wavelength, incidence angle, and sensor-to-target distance, respectively.

The high accuracy is due to the use of a very high-resolution DSM which accurately subtracted the topography from interferograms and from the choice we made to work with the residual height and manually add the height of the reference point instead of creating a DSM and a DTM to make the subtraction between them. In a further discussion, the residual height results from the discarded topographic component of the interferometric phase with the use of an external DEM. Since most geometric components of the phase in urban areas are generated by the height of buildings, the higher the resolution of the external DEM, the more accurate the residual height estimation will be. This is to say that using a coarse external DEM over urban areas is pointless because it is impossible to approach a good accuracy in building height estimation.

5. Conclusions

The proposed method is an efficient way to detect newly constructed buildings and estimate their heights based on open-domain Sentinel-1 SAR images and the PSI technique. Most new buildings in the study area were detected and their number of stories was very accurately determined. In urban planning, knowing the number of stories is as, if not more, important than knowing the absolute height of the building. The role of the residual height parameter and the setting of the corresponding reference point is crucial in the detection procedure. Overall, the results concerning the new building detection were sufficient and can be applied to monitor and study change detection in cities. While the method is efficient for urban areas, the efficiency is reduced when the area does not present a detached planning system, since the objective is per-building detection. This is to say that in some cases, the method cannot distinguish between two adjoining attached buildings (having one or more sides connected by a common wall or walls) due to the moderate resolution of Sentinel-1. Very high-resolution data would be more suitable, but currently no such data are available as open domain. Our intention for the future is to test the method with high-resolution data such as Cosmosky-Med and TerraSAR-X.

Author Contributions: Conceptualization, V.L., I.F. and D.S.; Methodology, V.L.; Validation, V.L.; Writing–original draft, V.L. and D.S.; Visualization, V.L.; Supervision, D.S. All authors have read and agreed to the published version of the manuscript.

Funding: This research is co-financed by Greece and the European Union (European Social Fund-ESF) through the Operational Program «Human Resources Development, Education and Lifelong Learning» in the context of the project "Strengthening Human Resources Research Potential via Doctorate Research" (MIS-5000432), implemented by the State Scholarships Foundation (IKϒ).

Data Availability Statement: Publicly available datasets were analyzed in this study. Sentinel-1 data are available via the Copernicus Open Science Hub (https://scihub.copernicus.eu, accessed on 8 June 2022) and the cadastral land parcels are available via the INSPIRE Geoportal of the Hellenic Cadastre (https://www.ktimanet.gr/geoportal/catalog/main/home.page, accessed on 8 June 2022).

Acknowledgments: This work has made use of data from the European Space Agency (ESA) through the Sentinel-1 mission. The authors would like to thank the SARPROZ team for providing their valuable software for research purposes. Pleiades-1B tri-stereo raw data were delivered under the supersite «Enceladus Supersite Goals» initiative via the Enceladus partner GEOSYSTEMS HELLAS SA.

Conflicts of Interest: The authors declare no conflict of interest.

References

1. Alaloul, W.S.; Musarat, M.A.; Rabbani, M.B.A.; Iqbal, Q.; Maqsoom, A.; Farooq, W. Construction Sector Contribution to Economic Stability: Malaysian Gdp Distribution. *Sustainability* **2021**, *13*, 5012. [CrossRef]
2. Stathakis, D.; Tsilimigkas, G. Measuring the Compactness of European Medium-Sized Cities by Spatial Metrics Based on Fused Data Sets. *Int. J. Image Data Fusion* **2015**, *6*, 42–64. [CrossRef]
3. Triantakonstantis, D.; Stathakis, D. Examining Urban Sprawl in Europe Using Spatial Metrics. *Geocarto Int.* **2015**, *30*, 1092–1112. [CrossRef]
4. Pramanik, M.M.A.; Stathakis, D. Forecasting Urban Sprawl in Dhaka City of Bangladesh. *Environ. Plan. B Plan. Des.* **2016**, *43*, 756–771. [CrossRef]
5. Stathakis, D.; Vasilakos, A. Comparison of Computational Intelligence Based Classification Techniques for Remotely Sensed Optical Image Classification. *IEEE Trans. Geosci. Remote Sens.* **2006**, *44*, 2305–2318. [CrossRef]
6. Stathakis, D.; Perakis, K.; Savin, I. Efficient Segmentation of Urban Areas by the VIBI. *Int. J. Remote Sens.* **2012**, *33*, 6361–6377. [CrossRef]
7. Stathakis, D.; Perakis, K. Feature Evolution for Classification of Remotely Sensed Data. *IEEE Geosci. Remote Sens. Lett.* **2007**, *4*, 354–358. [CrossRef]
8. Stathakis, D.; Kanellopoulos, I. Global Elevation Ancillary Data for Land-Use Classification Using Granular Neural Networks. *Photogramm. Eng. Remote Sens.* **2008**, *74*, 55–63.
9. Ferretti, A.; Prati, C.; Rocca, F. Permanent Scatterers in SAR Interferometry. *IEEE Trans. Geosci. Remote Sens.* **2001**, *39*, 8–20. [CrossRef]
10. Chini, M.; Pelich, R.; Hostache, R.; Matgen, P.; Lopez-Martinez, C. Towards a 20 m Global Building Map from Sentinel-1 SAR Data. *Remote Sens.* **2018**, *10*, 1833. [CrossRef]
11. Balz, T.; Washaya, P.; Jendryke, M. Urban Change Monitoring Using Globally Available Sentinel-1 Imagery. In Proceedings of the 2018 International Workshop on Big Geospatial Data and Data Science (BGDDS), Wuhan, China, 22–23 September 2018; pp. 1–4.
12. Cao, H.; Zhang, H.; Wang, C.; Zhang, B. Operational Built-up Areas Extraction for Cities in China Using Sentinel-1 SAR Data. *Remote Sens.* **2018**, *10*, 874. [CrossRef]
13. Yang, C.H.; Pang, Y.; Soergel, U. Monitoring of Building Construction by 4D Change Detection Using Multi-Temporal SAR Images. *ISPRS Ann. Photogramm. Remote Sens. Spat. Inf. Sci.* **2017**, *4*, 35–42. [CrossRef]
14. Li, L.; Wang, C.; Zhang, H.; Zhang, B. Residual Unet for Urban Building Change Detection with Sentinel-1 SAR Data. In Proceedings of the IGARSS 2019—2019 IEEE International Geoscience and Remote Sensing Symposium, Yokohama, Japan, 28 July–2 August 2019; pp. 1498–1501.
15. Zhang, J.; Cui, M.; Wang, B.; Chen, C.; Zhou, Y.; Li, J. A Novel SAR Images Change Detection Method Based on Dynamic TUNET-CRF Model. In Proceedings of the 2021 IEEE International Conference on Smart Internet of Things (SmartIoT), Jeju Island, Korea, 13–15 August 2021; pp. 107–111.
16. Hafner, S.; Nascetti, A.; Azizpour, H.; Ban, Y. Sentinel-1 and Sentinel-2 Data Fusion for Urban Change Detection Using a Dual Stream U-Net. *IEEE Geosci. Remote Sens. Lett.* **2022**, *19*, 9856. [CrossRef]
17. Jaturapitpornchai, R.; Matsuoka, M.; Kanemoto, N.; Kuzuoka, S.; Ito, R.; Nakamura, R. Newly Built Construction Detection in SAR Images Using Deep Learning. *Remote Sens.* **2019**, *11*, 1444. [CrossRef]
18. Pirrone, D.; De, S.; Bhattacharya, A.; Bruzzone, L.; Bovolo, F. An Unsupervised Approach to Change Detection in Built-Up Areas by Multitemporal PolSAR Images. *IEEE Geosci. Remote Sens. Lett.* **2020**, *17*, 1914–1918. [CrossRef]
19. Jing, H.; Sun, X.; Wang, Z.; Chen, K.; Diao, W.; Fu, K. Fine Building Segmentation in High-Resolution SAR Images Via Selective Pyramid Dilated Network. *IEEE J. Sel. Top. Appl. Earth Obs. Remote Sens.* **2021**, *14*, 6608–6623. [CrossRef]
20. Connetable, P.; Conradsen, K.; Nielsen, A.A.; Skriver, H. Test Statistics for Reflection Symmetry: Applications to Quad-Polarimetric SAR Data for Detection of Man-Made Structures. *IEEE J. Sel. Top. Appl. Earth Obs. Remote Sens.* **2022**, *15*, 2877–2890. [CrossRef]

21. Zhu, F.; Zhang, Y.; Li, D. A Novel Polarimetric Interferometric SAR Coherence Parameter and Its Application in Buildings Detection. In Proceedings of the 2016 Progress in Electromagnetics Research Symposium, PIERS 2016 Proceedings, Shanghai, China, 3 November 2016; pp. 1730–1733.
22. Marin, C.; Bovolo, F.; Bruzzone, L. Building Change Detection in Multitemporal Very High Resolution SAR Images. *IEEE Trans. Geosci. Remote Sens.* **2015**, *53*, 2664–2682. [CrossRef]
23. Liu, L.; Zhang, F.; Wu, Q.; Wang, G. Building Footprint Extraction by Fusing Dual-Aspect SAR Images. In Proceedings of the 2011 IEEE International Geoscience and Remote Sensing Symposium, Vancouver, BC, Canada, 24–29 July 2011; pp. 1866–1869.
24. Ferro, A.; Brunner, D.; Bruzzone, L. Automatic Detection and Reconstruction of Building Radar Footprints From Single VHR SAR Images. *IEEE Trans. Geosci. Remote Sens.* **2013**, *51*, 935–952. [CrossRef]
25. Rapuzzi, A.; Nattero, C.; Pelich, R.; Chini, M.; Campanella, P. CNN-Based Building Footprint Detection from Sentinel-1 SAR Imagery. In Proceedings of the International Geoscience and Remote Sensing Symposium (IGARSS), Waikoloa, HI, USA, 26 September 2020; pp. 1707–1710.
26. Cao, Y.; Su, C.; Yang, G. Detecting the Number of Buildings in a Single High-Resolution SAR Image. *Eur. J. Remote Sens.* **2014**, *47*, 513–535. [CrossRef]
27. Koppel, K.; Zalite, K.; Sisas, A.; Voormansik, K.; Praks, J.; Noorma, M. Sentinel-1 for Urban Area Monitoring-Analysing Local-Area Statistics and Interferometric Coherence Methods for Buildings' Detection. In Proceedings of the International Geoscience and Remote Sensing Symposium (IGARSS), Milan, Italy, 10 November 2015; pp. 1175–1178.
28. Perissin, D.; Ferretti, A. Urban-Target Recognition by Means of Repeated Spaceborne SAR Images. *IEEE Trans. Geosci. Remote Sens.* **2007**, *45*, 4043–4058. [CrossRef]
29. Crosetto, M.; Monserrat, O.; Cuevas-González, M.; Devanthéry, N.; Crippa, B. Persistent Scatterer Interferometry: A Review. *ISPRS J. Photogramm. Remote Sens.* **2016**, *115*, 78–89. [CrossRef]
30. Panagiotakis, E.; Chrysoulakis, N.; Charalampopoulou, V.; Poursanidis, D. Validation of Pleiades Tri-Stereo DSM in Urban Areas. *ISPRS Int. J. Geoinf.* **2018**, *7*, 118. [CrossRef]
31. Perissin, D.; Rocca, F. High-Accuracy Urban DEM Using Permanent Scatterers. *IEEE Trans. Geosci. Remote Sens.* **2006**, *44*, 3338–3347. [CrossRef]
32. Colesanti, C.; Ferretti, A.; Perissin, D.; Prati, C.; Rocca, F. Evaluating the Effect of the Observation Time on the Distribution of SAR Permanent Scatterers. In Proceedings of the FRINGE 2003, Frascati, Italy, 1–5 December 2003; Volume ESA SP-550.
33. Ferretti, A.; Perissin, D.; Prati, C. Spaceborne SAR Anatomy of a City. In Proceedings of the FRINGE 2005, Frascati, Italy, 28 November–2 December 2005.
34. Perissin, D.; Prati, C.; Engdahl, M.E.; Desnos, Y.L. Validating the SAR Wavenumber Shift Principle With the ERS–Envisat PS Coherent Combination. *IEEE Trans. Geosci. Remote Sens.* **2006**, *44*, 2343–2351. [CrossRef]
35. Perissin, D.; Wang, T. Repeat-Pass SAR Interferometry with Partially Coherent Targets. *IEEE Trans. Geosci. Remote Sens.* **2012**, *50*, 271–280. [CrossRef]
36. Perissin, D. 2.04—Geometric Processing: Active Sensor Modeling and Calibration (SAR). In *Comprehensive Remote Sensing*; Liang, S., Ed.; Elsevier: Oxford, UK, 2018; pp. 61–76. ISBN 978-0-12-803221-3.

Disclaimer/Publisher's Note: The statements, opinions and data contained in all publications are solely those of the individual author(s) and contributor(s) and not of MDPI and/or the editor(s). MDPI and/or the editor(s) disclaim responsibility for any injury to people or property resulting from any ideas, methods, instructions or products referred to in the content.